Can full waveform inversion image all scales of the velocity model?

Biondo Biondi, Ettore Biondi, and Guillaume Barnier

ABSTRACT

Full waveform inversion (FWI) reconstructs the velocity model based on the information contained in reflections and diving waves, in addition to a tomographic component that contributes when reflected events are not well focused. The wavenumber-domain analysis of the contributions of each of these elements shows that they are mostly complementary. The illumination patterns in the wavenumber domain are scaled by the data frequency, further expanding the wavenumber-domain region that is illuminated by reflections data. When cycle-skipping is not occurring, FWI applied to wideband data should be able to reconstruct all the scales of the velocity model. Our tests on synthetic datasets support this analysis; however, they also show that FWI applied to wideband data (2.5-30 Hz) with long offsets (up to 9km) is not able to reconstruct a small region of the wavenumber plane close to the origin. For our specific examples, the poorly reconstructed scales have vertical wavelengths longer than 400 m and horizontal wavelengths between 150 m and 600 m.

INTRODUCTION

The ultimate goal of seismic imaging is to image all scales of the subsurface velocity model. Full waveform inversion (FWI) aims to extract the information that is contained in the data for all the scales of the model. FWI estimates are more reliable for some scales (short wavelengths) than for others (long wavelengths) because of "cycle skipping" caused by the non-linearity of the wave equation with respect to the model parameters. To better understand the challenge, and possibly devise more robust inversion algorithms, we analyze the contributions to the process of imaging different scales of the model by different data components. In particular we analyze the contributions by: 1) reflections, 2) diving (overturned) waves, and 3) a tomographic component that is related to reflections focusing (reflection tomography). These last two categories are linked to transmission (forward-scattered) effects, whereas the first one is linked to reflection (back-scattered) effects.

Our analysis is based on the "classic" graphic understanding of the model wavenumber illumination provided by single-scattered data as a function of the recording geometry that has been presented by Wu and Toksoz (1987). Their analysis is based

on the assumption of single scattering in a constant medium background, but it provides a good starting point to analyze diving waves that are recorded only when the background model increases with depth. More challenging is the analysis of the reflection-tomography contributions that come into play only when the background model contains scatterers. The single-scattering framework can be extended to provide a qualitative understanding of the illumination provided by reflection tomography. However, the wavenumber components that are illuminated by reflection tomography are not only dependent on the scattering geometry, but also on the wavenumber content of the the imaged reflector in the background model. Therefore, we think that a more complete theory that formally explains double-scattered events should be developed to quantitatively analyze the illumination provide by reflection tomography.

To illustrate and validate our analysis we modeled three synthetic datasets and imaged them by FWI. These datasets were modeled assuming random velocity perturbations superimposed onto a linearly increasing background model. The random perturbations for the first dataset were generated assuming a uniform distribution with zero mean and variance of 1.5 m/s. To generate the other two datasets we scaled these random perturbations by a factor of 10 and 20. Because of the low-frequency content of the source function, FWI converges for all three datasets.

MODEL-SCALES ILLUMINATED BY REFLECTION SEISMIC DATA

Wu and Toksoz (1987) introduced a simple graphical method to analyze the illumination of the seismic experiment as a function of acquisition geometry. The method is based on a single-scattering assumption and on plane-waves decomposition of the wavefields. Figures 1 and 2 summarize the basic idea. Figure 1 shows an incident plane wave (red) propagating downward at an angle α with respect to the vertical direction. Subsurface heterogeneities scatter back the incident plane wave. The scattered wavefield can be decomposed into its plane-waves components. The Figure represents one of them (green) propagating back towards the surface at an angle β with respect to the vertical direction. The angle γ is the scattering angle for these two plane waves. Figure 2 shows the corresponding wavenumber representation of the scattering phenomenon represented in Figure 1. If we assume the plane waves to be monochromatic, we can represent them as the vectors $\mathbf{k}_s$ and $\mathbf{k}_g$ in the wavenumber plane as follows:

$$\begin{aligned} \mathbf{k}_s &= \frac{\omega_0}{V_0}\left(\sin\alpha\mathbf{k}_x - \cos\alpha\mathbf{k}_z\right), \\ \mathbf{k}_g &= \frac{\omega_0}{V_0}\left(\sin\beta\mathbf{k}_x - \cos\beta\mathbf{k}_z\right), \end{aligned} \tag{1}$$

where $\mathbf{k}_x$ and $\mathbf{k}_y$ are the unit vectors along the wavenumber axes, ω_0 is the angular frequency of the plane waves, and V_0 is the constant velocity of the medium. The

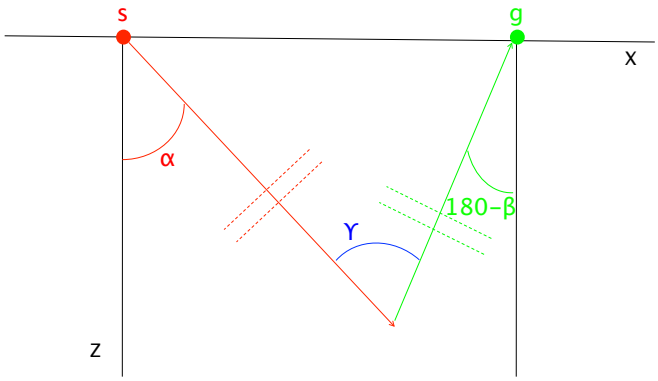

Figure 1: The incident plane wave (red) generated by the source(s) propagates downward at an angle α with respect to the vertical. The scattered wavefield can be decomposed into several plane waves; one of them (green) propagates back towards the surface at an angle β with respect to the vertical. The angle γ is the scattering angle for these two plane waves. [**NR**].

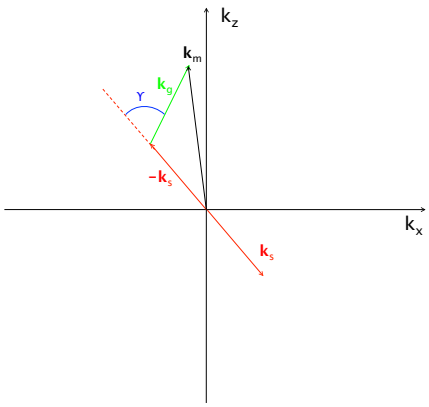

Figure 2: Wavenumber representation of the plane-waves scattering phenomenon represented in Figure 1, accordingly to equations 1 and 2. [**NR**].

model wavenumber vector $\mathbf{k}_m$ (black in the Figure) illuminated by the data component corresponding to the scattered plane wave is equal to

$$\mathbf{k}_m = \mathbf{k}_s - \mathbf{k}_g. \tag{2}$$

Figure 2 shows also the scattering angle γ as a function of the wavenumber-domain vectors.

Figure 3 shows the region of the model space that are illuminated by a single frequency, for all possible angles α and β. The circumference of the large gray circle corresponds to the normal-incidence reflections, which are the highest-resolution events that can be recorded at ω_0. The orange circle is the region of the wavenumber plane that is illuminated by forward-scattered plane waves; that is, scattered plane waves for which $90^o \leq \gamma \leq 270^o$. We will refer to these events as transmission events.

The light-blue circles on the side, and partially covered by the orange circle, are the regions of the wavenumber plane that require the vertical wavenumber of the incident and scattered plane waves to have the same sign. This condition is equivalent to the

condition that the incident plane wave and the scattered plane wave are traveling along the same vertical direction. In a constant velocity background and under the assumption of single scattering, these plane waves cannot be recorded by seismic data acquired at the surface. Therefore, conventional reflections (that is back-scattered energy recorded at the surface) can only illuminate the regions of the gray circle that are not covered by the orange and light-blue circles.

However, if in addition to reflections we record also diving waves caused by a background model with increasing velocity with depth, we can illuminate an additional region of the wavenumber plane. The part of the orange circle visible in Figure 4 shows the region of the wavenumber plane that can be illuminated by diving waves. The recorded data are forward scattered and the incident and scattered energy propagate along the same horizontal direction, but opposite vertical directions (at least with a constant velocity background; in the presence of a vertical gradient this condition does not need to be exactly fulfilled).

Second-order scattering illuminates an additional region of the wavenumber plane. These contributions are present in the FWI gradients if the background model contains sufficient short-wavelength heterogeneity to cause substantial back scattering, as typically happens for FWI iterations after the first one. We can consider this term the "reflection tomography" component of seismic imaging. Reflection tomography illuminates the regions of the orange circle that are visible in Figure 5. These wavenumber components are illuminated by forward scattered energy for which the incident and scattered plane waves propagate along the same vertical direction, either downward for the source wavefield, or upward for the receiver wavefield. When the source plane wave is scattered, the incident wavenumber vector points down (upward for $-\mathbf{k}_s$ in Figure 5) and the scattered wavenumber vector ($\mathbf{k}_{s'}$ in the Figure) points downward. Conversely, when the reflected plane wave is scattered, the incident wavenumber vector $\mathbf{k}_g$ points up, and the scattered wavenumber vector $\mathbf{k}_{g'}$ points upward. It should be noted that the reflection tomography contribution not only depends on the presence of reflectors in the background model, but also that it depends on their orientation and frequency content.

The transmission components (diving waves and reflection tomography) are the most prone to cycle skipping when the background model is far from the correct one. Common workflows based on ray-tracing tomography are usually capable to estimate starting models that avoid cycle skipping of diving waves arrival. In contrast, ray-tracing tomography is less likely to yield sufficiently accurate models to avoid cycle skipping in the reflection-tomography FWI component.

Figure 6 shows the same circles shown in Figure 3 with their copies, scaled down by a factor of two, superimposed onto them. These smaller circles correspond to plane waves with half the frequency of the previous one; that is, $\omega_h = \omega_0/2$. When we record wideband data (i.e. $\omega_h \leq \omega \leq \omega_0$) the different data components (reflections, diving waves, and reflection tomography) illuminate the regions of the wavenumber plane that are swept as the circles continuously expand from the small ones to the large ones, as indicated by the blue arrows in Figure 6.

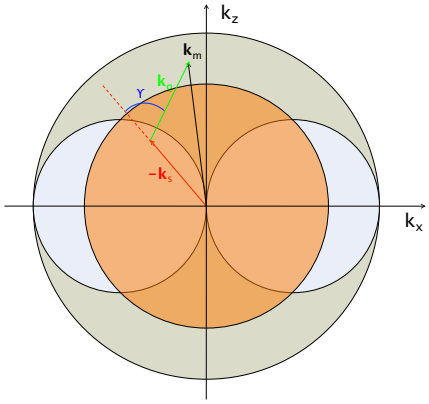

Figure 3: The regions of the model space that are illuminated by a single frequency, for all possible angles α and β. The gray areas are illuminated by surface data with reflections. The orange circle is illuminated by forward-scattered plane waves. The light-blue areas cannot be illuminated by surface data. [**NR**].

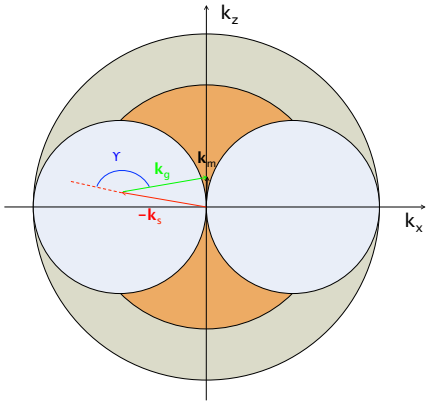

Figure 4: The portion of the orange circle not covered by the light-blue circles is illuminated by diving waves recorded by long-offset surface data when the velocity increases with depth. [**NR**].

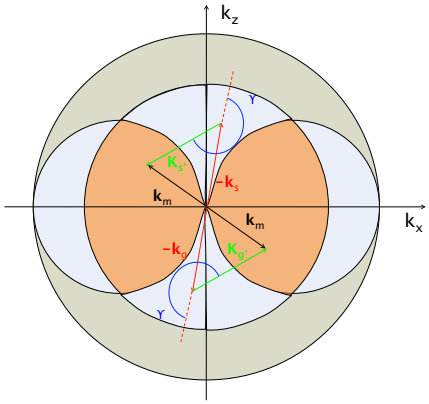

Figure 5: The portion of the orange circle not covered by the light-blue circles is illuminated by the "reflection tomography" component of the data. It is present in the FWI gradients when the background model contains scatterers as typically happens for FWI iterations after the first one. [**NR**].

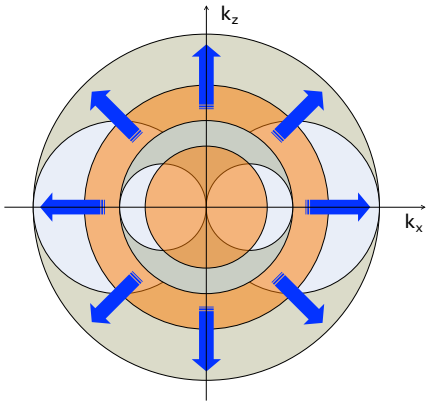

Figure 6: The circles shown in Figure 3 with their copies scaled down by a factor of two superimposed onto them. These smaller circles correspond to plane waves with half the frequency of the previous one. Wideband data illuminate the regions of the wavenumber plane that are swept as the circles continuously expand from the small ones to the large ones. [**NR**].

SYNTHETIC EXAMPLE

To illustrate the concepts presented in the previous section we modeled three synthetic datasets assuming random perturbations superimposed onto a background model with velocity linearly increasing with depth; the background velocity was defined as $v(z) = (1 + 0.44z)$ km/s. Because velocity increases with depth, this background model creates overturned events. The random perturbations for the first dataset (#1) were generated assuming a uniform distribution with zero mean and variance of 1.5 m/s. The other datasets were generated using the same random perturbations scaled up by a factor of 10 (#2) and 20 (#3). The random perturbations ensure that the perturbed model is different from zero at all the wavenumbers. We modeled 48 sources equally spaced 150 m apart. The receiver array was 10 km wide and stationary for all sources. Figure 7 shows that the spectrum of the sources is different from zero between 2.5 Hz and 30 Hz. The spatial grid was 10 m in both directions; therefore the Nyquist wavenumber was .05 m^{-1}.

First-iteration FWI images

Figure 8a shows the search direction at the first iteration of a FWI process applied to dataset #1; we can clearly see the contributions of the reflected events and the diving waves superimposed onto each other. To help distinguish these two types of contributions to the search directions we approximately separated the corresponding events in the data domain by applying a linear muting as a function of offset that removed the diving waves from the data. Figure 8b shows the search direction computed by back-projecting the muted residuals, whereas Figure 8c shows its complement; that is, the search direction corresponding to the diving waves.

Figure 9 shows the wavenumber spectra computed from the images shown in Figure 8. The shape of these wavenumber spectra fits the graphical analysis presented

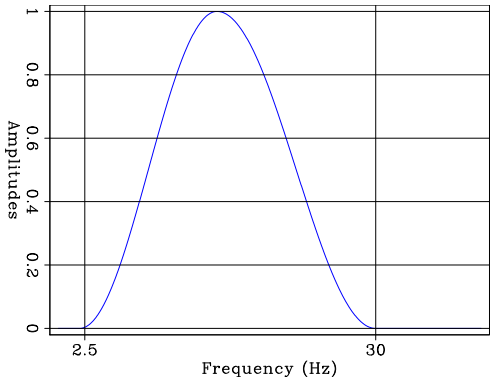

Figure 7: Frequency spectrum of the wavelet used to model the datasets. [**CR**]

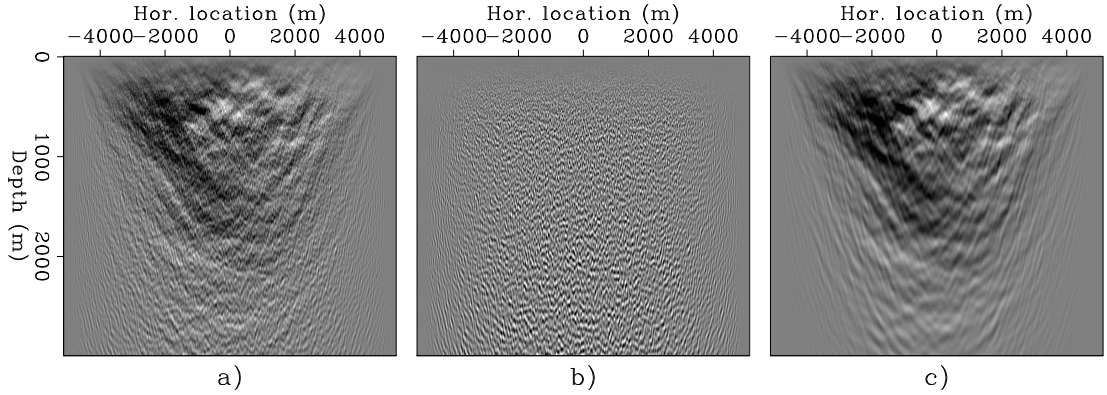

Figure 8: Search directions at the first iteration of a FWI process applied to dataset #1. To produce panel a) all components of the data (reflections and diving waves) are backprojected into the model. To produce panels b) and c) reflections (b) and diving wave (c) are separately backprojected into the model. [**CR**]

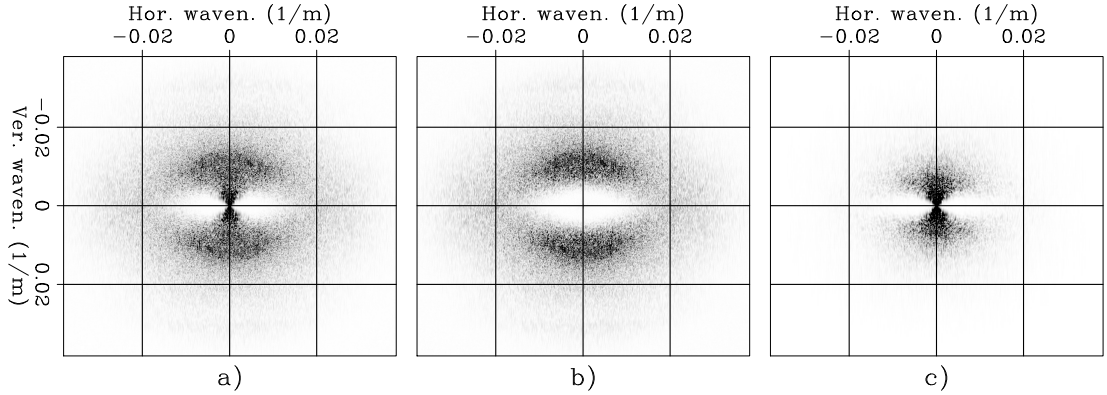

Figure 9: Wavenumber spectra computed from the images shown in Figure 8 and corresponding to a) reflections and diving waves, b) reflections, and c) diving waves. [**CR**]

in Figures 3 and 4. The characteristic eye-glasses that correspond to the light-blue circles in Figure 4 are clearly visible in Figure 8a as areas of amplitudes close to zero. As graphically illustrated by Figure 6, because the sources were wideband these circles are stretched horizontally and their borders are fuzzy.

For dataset #1 the velocity perturbations are very small; therefore, we expect the images shown in Figure 8 are good approximations of the true perturbations within the respective wavenumber regions. Figures 10a and 10b compare the bandpassed true perturbations to the imaged reflections, respectively. To facilitate the comparison Figure 10b shows the same image as shown in Figure 8b. To generate Figure 10a we applied a mask in the wavenumber domain that was designed to attenuate all the wavenumbers except within the region where we would expect the reflected events to be imaged. We can notice that wherever the random perturbations align to create semi-coherent events, these events are consistent between the two displays. Because velocity increases with depth the wavelengths increase with depth in the image (Figure 10b). Furthermore, because of the limitations of a surface-bound acquisition geometry, the angular bandwidth drastically decreases with depth in the actual image (Figure 10b).

Figure 10c shows the wavenumber spectrum of the image shown in Figure 10a and has similarities with Figure 9b. The lower amplitudes at high horizontal wavenumbers in Figure 9b with respect to Figure 10c are caused by the loss of angular bandwidth with depth.

Similarly to Figure 10, Figure 11 compares bandpassed true perturbations to the imaged diving waves, respectively. In the shallow section there is an approximate correspondence between the imaged velocity anomalies and the true bandpassed perturbations. Figure 11c shows the wavenumber spectrum of the image shown in Figure 11a. As for the previous Figure, to facilitate the comparison between the bandpassed true perturbations and the estimated image, Figure 11b shows the same image as shown in Figure 8c.

Second-iteration FWI images

From the analysis presented in the previous section, we would expect that at the second iteration of a FWI procedure the reflection-tomography component of the gradient will fill some of the wavenumber-components missing from the images after the first iteration. Figure 12 shows the effects of the reflection-tomography component when FWI is applied to dataset #2. Figure 12b shows the search direction of the second iteration of FWI after applying a lowpass filter in the wavenumber domain to remove the most of the reflection components from the image. This image was generated by back-projecting the residuals after applying a linear mute to remove the diving-waves arrivals. We applied the same mute that we applied to the first-iteration residuals to generate the reflection image shown in Figure 8b. The muting of the residuals and the lowpass of the image were applied to isolate the reflection-

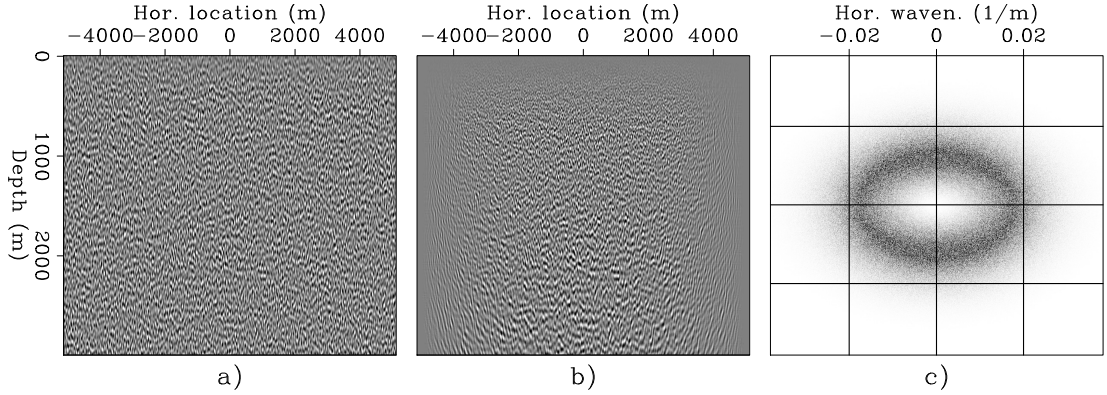

Figure 10: Bandpassed true perturbations (panel a) compared to the imaged reflections (panel b). Wherever the random perturbations align to create semi-coherent events, these events are consistent between the two images. Panel c) shows the wavenumber spectrum of panel a). [**CR**]

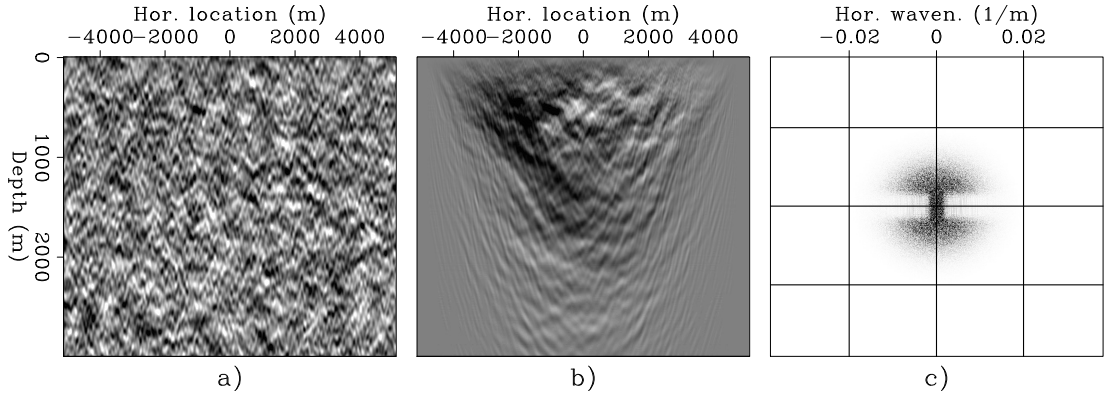

Figure 11: Bandpassed true perturbations (panel a) compared to the imaged diving waves (panel b). In the shallow section there is an approximate correspondence between the imaged velocity anomalies and the true bandpassed perturbations. Panel c) shows the wavenumber spectrum of panel a). [**CR**]

tomography contributions as much as possible. These contributions tend to have lower amplitudes and would be easily missed if not isolated from the stronger contributions of the reflections and diving waves.

Figure 12a shows the true perturbations after applying the same lowpass filter applied to the second-iteration search direction. Comparing Figure 12a with Figure 12b we can match several narrow velocity anomalies. These anomalies are better resolved in the reflection-tomography image than in the corresponding diving-waves image obtained at the first iteration of FWI applied to dataset #1 (Figure 12c.) This increase in lateral resolution is reflected in the wavenumber spectrum of the reflection-tomography image that is shown in Figure 13a. The spectra corresponding to the reflections and diving-waves images obtained after the first iteration are shown again in Figure 13b and 13c. This example shows that the contribution of reflection tomography is complementary to the one of diving waves and reflections. However, it also shows that a smaller region of the wavenumber plane is illuminated by the reflection tomography component than we would have expected from the graphic analysis presented in the previous section.

Figure 14 compares the lowpassed second-iteration search directions obtained for datasets #1, #2, and #3. Multiple scattering caused by the random velocity perturbations causes a slow down of the recorded reflections and causes the reflection-tomography component of the velocity updates at the second iteration to be biased towards negative updates. Because the kinematic error is very small for dataset #1 the image in Figure 14a is contaminated by reflections. In contrast, the stronger multiple-scattering caused by the larger velocity perturbations in datasets #2 and #3 causes an overall slow down of the recorded reflections and thus it enhances the tomographic component. Figure 14c shows similar features as Figure 14b, but it is more biased towards negative velocity updates because events are slowed down by multiple-scattering more in dataset #3 than in dataset #2.

FWI images

When we perform many iterations of FWI on the whole data; that is, without separating reflections from diving waves as in the experiments shown above, all the three components analyzed above (reflections, diving waves and reflection tomography) simultaneously contribute to the inversion process. If the initial velocity error is sufficiently small, the FWI process converges to an optimal model that approximates the true model for all the wavenumbers that are illuminated by the data.

Figure 15 shows the results of applying FWI to all the data components (reflections and diving waves) for dataset #1 after 10, 50, and 150 iterations of FWI using a BFGS solver. Figure 16 shows the wavenumber spectra of the models shown in Figure 15. The first 10 iterations solve for the shallow long-wavelength anomalies, mostly driven by the diving waves in the data. Iterations between 10 and 50 reach to the deeper part of the model and start to bring up the short wavelengths directly illuminated by

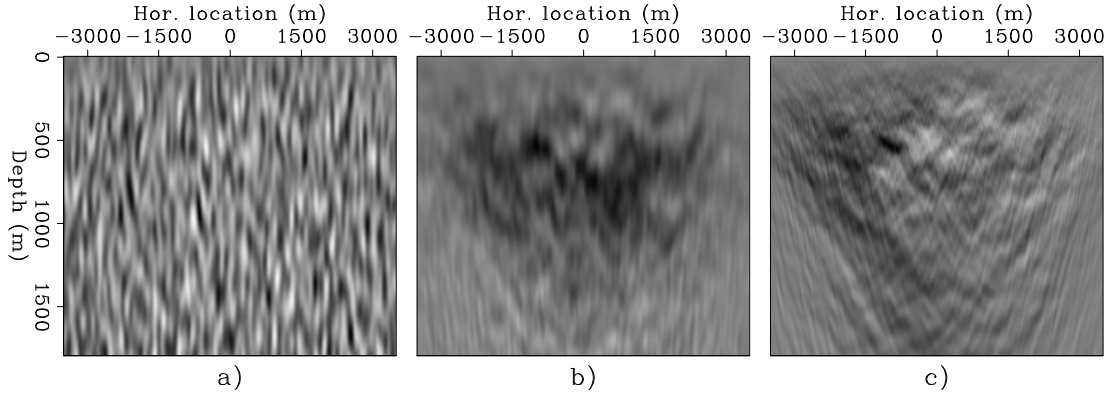

Figure 12: Bandpassed true perturbations (panel a) compared to the "reflection tomography" contributions to the second search direction of a FWI process (panel b). Panel c) shows the shallow part of the image obtained from the first iteration of FWI applied to diving waves in dataset #1. (Figure 11b.) [**CR**]

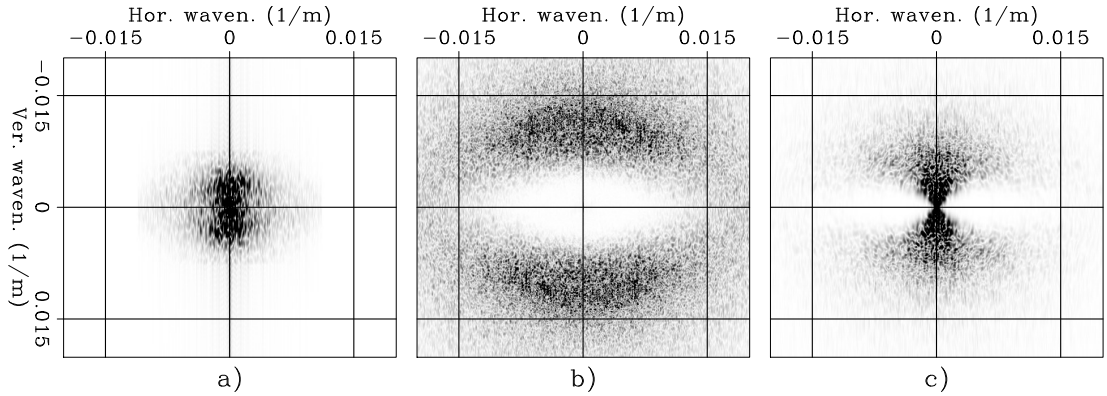

Figure 13: Wavenumber spectra computed from the images shown in: a) Figure 12b, b) Figure 8b, and c) Figure 8c. [**CR**]

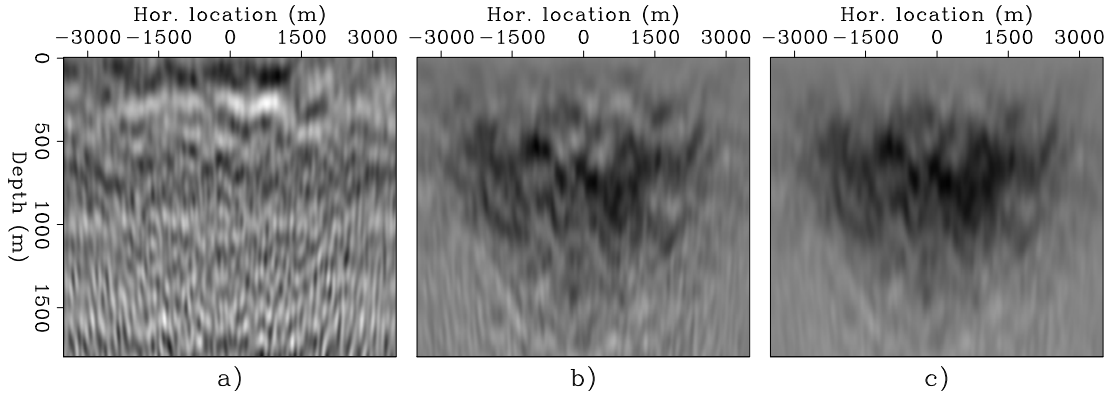

Figure 14: Figure 14 compares the lowpassed second-iteration search directions obtained by applying FWI to datasets #1, #2, and #3. Notice the increasing (left to right) bias towards negative updates related to the slow down caused by increasing multiple scattering in the data. [**CR**]

the reflections. The last 100 iterations equalize the amplitudes of the model in depth and across the wavenumbers by resolving some of the intermediate wavelengths at deeper depths.

The spectral holes with the shape of eyeglasses are squeezed by the the later FWI iterations compared to the first ones. However, they are persistent indicating that there are some wavelengths of the model that cannot be resolved from the surface data even in presence of low frequencies, large offsets, and a vertical velocity gradient. Figure 17 shows windows around the origin of the spectra shown in Figure 16. It shows that the FWI process has not resolved model components with vertical wavelengths longer than 400 m and horizontal wavelengths between 150 m and 600 m.

DISCUSSIONS AND FUTURE WORK

The graphic analysis of the wavenumber illumination by reflections, diving waves, and reflection tomography shows that FWI has the potential to image all scales of the velocity model, if cycle-skipping does not occur. However, the synthetic-data examples shows that there is a region of the wavenumber plane that is not illuminated by the data. The most likely culprit for this limitation is that reflection tomography does not resolve all the wavenumbers that the graphic analysis we presented would indicate. A more complete theory that formally explains double-scattered events should be developed to quantitatively analyze the illumination provide by reflection tomography and help develop methods to overcome this limitations.

REFERENCES

Wu, R. and M. N. Toksoz, 1987, Diffraction tomography and multisource holography applied to seismic imaging: Geophysics, **52**, 11–25.

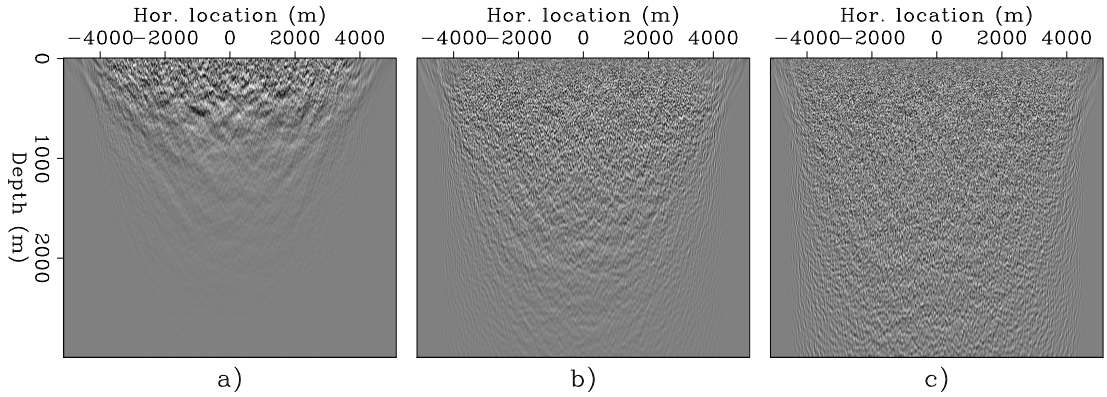

Figure 15: Velocity models obtained by FWI applied to dataset #1 after: a) 10 iterations, b) 50 iterations, and c) 150 iterations. [**CR**]

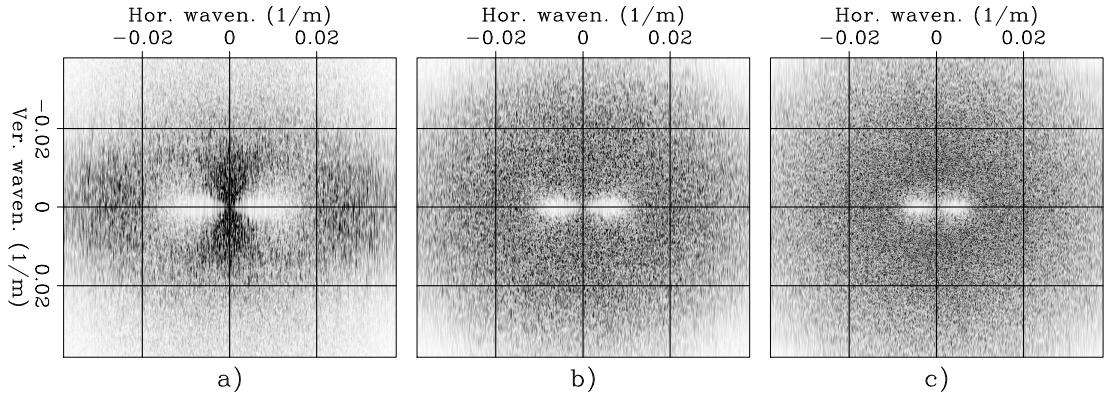

Figure 16: Wavenumber spectra of the velocity models obtained by FWI applied to dataset #1 after: a) 10 iterations, b) 50 iterations, and c) 150 iterations. [**CR**]

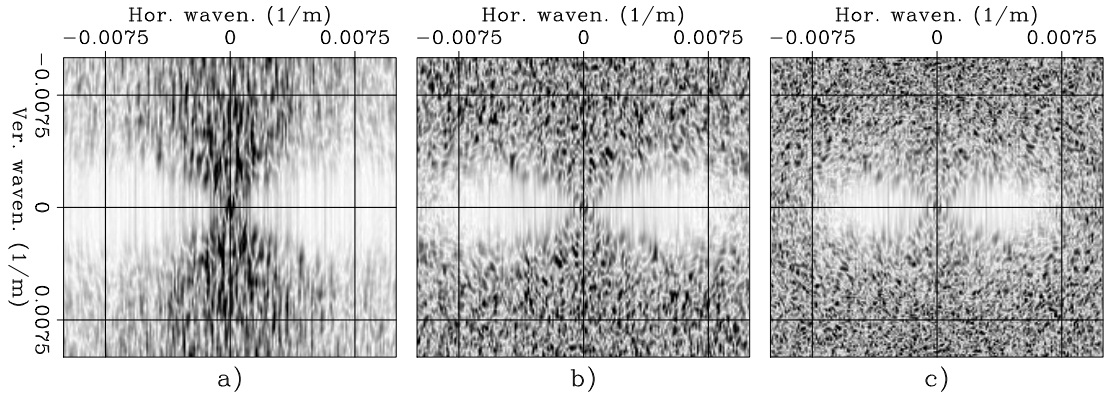

Figure 17: Windows of the wavenumber spectra shown in Figure 16 that focuses on the area of the wavenumber plane that are least resolved by the FWI process. [**CR**]